Supporting Information

Fluorine-Engineered Two-Dimensional Covalent Organic Frameworks for Enhanced C_2H_2/CO_2 Separation

Jialiang Liu, ‡[a] Wenjie Wei, ‡[a] Sen Wang,[a] Pengyue Hao,[a] Wang Zhang,[a] Yongwu Peng*[a,b]

[a] College of Materials Science and Engineering, Science and Education Integration College of Energy and Carbon Neutralization, Zhejiang University of Technology, Hangzhou 310014, China
[b] School of Materials Science and Chemical Engineering, Ningbo University, Ningbo 315211, China.
E-mail: ywpeng@zjut.edu.cn, pengyongwu@nbu.edu.cn
‡ These authors contributed equally to this work.

Table of Contents

1. Materials and methods

2,6-difluoro-4-(4,4,5,5-tetramethyl-1,3,2-dioxaborolan-2-yl)aniline, 2,4,6-trihydroxybenzene-1,3,5-tricarbaldehyde, 1,3,5-trifluoro-2,4,6-triiodobenzene were purchased from Shanghai Tensus Biotech Co., Ltd. $Pd(pph_3)_4$, $Pd(dppf)Cl_2$, K_2CO_3, 1,4-Dioxane, dichloromethane, ethyl acetate, petroleum ether, Mesitylene, N, N-dimethylacetamide (DMA, 99%), Dimethyl sulfoxide, 1,2-dichlorobenzene and Acetic Acid were purchased from Tokyo Chemical Industry Co., Ltd., All the materials were used as received without further purification.

Solution nuclear magnetic resonance (NMR): Liquid state ^1H nuclear magnetic resonance spectroscopy was collected on a Varian Mercury Plus 400 NMR Spectrometer.

Solid-state nuclear magnetic resonance (ssNMR): Solid-state nuclear magnetic resonance (NMR) data were performed on a Bruker AVANCE III 600 spectrometer with cross-polarization magic-angle-spinning (CP/MAS) at a resonance frequency of 150.9 MHz. ^{13}C CP/MAS NMR spectra were recorded using a 4 mm MAS probe and a spinning rate of 14 kHz. A contact time of 4 ms and a recycle delay of 2 s were used for the ^{13}C CP/MAS NMR measurement. The chemical shifts of ^{13}C were externally referenced to tetramethylsilane (TMS).

Fourier transform infrared (FT-IR): IR spectrum was measured on an IR spectrometer (Nicolet 6700) between the ranges of 4000 to 400 cm^{-1}.

Power X-ray diffraction (PXRD): PXRD patterns were collected on an X-ray diffraction (XRD) system (DX-27mini, China) using Cu Kα radiation.

Scanning electron microscopy (SEM): SEM images were collected using a GeminiSEM 500 system.

Transmission electron microscope (TEM): TEM images were obtained with a Tecnai G2 F30 STwin.

Thermogravimetric analysis (TGA): TGA was performed using a TA Q600. When under flowing N_2 atmosphere, the samples were heated in a Platinum pan (800 °C, 10 °C min^{-1}) under a N_2 flux (60 mL min^{-1}).

Sorption isotherm for N_2: Micrometrics ASAP2040 system were used to measure the specific surface area and pore structure using nitrogen as the adsorbate at 77 K, after outgassing the samples overnight at 120 °C.

Gas sorption: The samples were activated under vacuum for 12 hours at 120 °C. Gas adsorption experiments at 298 K were performed by using JW-BK200 surface area analyzer. A circulation constant temperature water bath was used to stabilize the temperature at 298 K during the test.

Crystal structure modeling: Crystal structure modeling: The unit cell parameters of the COFs were obtained from the indexing of the PXRD peaks using the Dicvol (Reflex module in the Materials

Studio program)[1], the structural modeling of COFs was generated using the Building (Crystal) module, the lattice model was geometrically optimized using force-filed based method (Forcite molecular dynamics module). The Pawley fitting (Reflex module) was performed to optimize the lattice parameters iteratively until the *R*wp value converges and the overlay of the observed with refined profiles shows good agreement.

Calculation of selectivity via ideal adsorption solution theory (IAST):

The gas adsorption isotherms were first fitted to a dual-site Langmuir-Freundlich (DSLF) model (eqn (3)), where is the amount of adsorbed gas q (mmol g^{-1}), P is the bulk gas phase pressure (atm), $qsat$ is the saturation amount (mmol g^{-1}), b is the Langmuir-Freundlich parameter ($atm^{-\alpha}$), and α is the Langmuir-Freundlich exponent (dimensionless) for two adsorption sites A and B indicating the presence of weak and strong adsorption sites.

$$q = q_{A,sat}\frac{b_A p}{1 + b_A p} + q_{B,sat}\frac{b_B p}{1 + b_B p} \quad (3)$$

IAST starts from the Raoult's Law type of relationship between the fluid and adsorbed phase (4) and (5), where P_i is the partial pressure of component i (atm), *P* is the total pressure (atm), and y_i and x_i represent mole fractions of component i in gas and the adsorbed phase (dimensionless). P_i^0 is the equilibrium vapour pressure (atm).

$$P_i = P y_i = P_i^0 x_i \quad (4)$$

$$\sum_{i=1}^{n} x_i = \sum_{i=1}^{n} \frac{P_i}{P_i^0} = 1 \quad (5)$$

In IAST, P is defined by relating to spreading pressure π (6), where π is the spreading pressure, S is the specific surface area of the adsorbent ($m^2\ g^{-1}$), R is the gas constant (8.314 J K^{-1} mol^{-1}), T is the temperature (K), and $q_i(P_i)$ is the single component equilibrium obtained from isotherms (mmol g^{-1}).

$$\frac{\pi S}{RT} = \int_0^{p^0} i\frac{q_i(P_i)}{P_i} \mathrm{d}p_i = \Pi(condtant) \quad (6)$$

For a DSLF model, we have an analytical expression for the integral (7). The isotherm parameters are derived from the previous fitting. For a binary component system, the unknowns will be Π, P, and which can be obtained by simultaneously solving eqn (5) and (7).

$$\int_0^{p^0} i\frac{q_i(P_i)}{P_i} \mathrm{d}p_i = \Pi(condtant) = \frac{q_{sat,A}}{a_A}\ln\left[1 + b_A (P_i^0)^{a_A}\right] + \frac{q_{sat,B}}{a_B}\ln\left[1 + b_B (P_i^0)^{a_B}\right] \quad (7)$$

The adsorbed amount of each compound in a mixture is (8) and (9), where q is the adsorbed amount of component (mmol g^{-1}), and is the total adsorbed amount (mmol g^{-1}).

$$q_i^{mix} = x_i q_t \quad (8)$$

$$\frac{1}{q_T} = \sum_{i=1}^{n} \frac{x_i}{q_i(P_i^0)} \quad (9)$$

The adsorption selectivities S_{ads} were calculated using eqn (10). In this study, IAST calculations were carried out assuming a binary mixed gas with a molar ratio of 50:50 at 298 K and pressures up to 1 atm.

$$S_{ads} = \frac{q_1/q_2}{p_1/p_2} \quad (10)$$

Water contact angle measurements：

Contact angle testing is performed by XG-CAMF. A drop of water (about 3 μL) is dropped onto the sample surface using a micro-injector, the droplet is captured by a high-resolution camera for automatic calculation of the contact angle by the system.

Isosteric heat of adsorption (Q_{st}):

The isosteric heats of adsorption were calculated using the Clausius-Clapeyron equation:

$$Q_{st} = -R \times \left[\frac{\partial ln(P)}{\partial(\frac{1}{T})}\right] \quad (11)$$

Where R is the gas constant constant (8.314 $J \cdot mol^{-1} \cdot K^{-1}$). Values of Qst were derived from the slopes of lnP versus 1/T plots at different adsorption loadings:

$$Q_{st} = -slope \times R \quad (12)$$

Density Functional Theory (DFT) Calculations:

In this work, all calculations are performed by the spin-unrestricted DFT method as implemented in Castep code of the Materials Studio package.[1] The electron exchange and correlation effects are described by Projector augmented wave (PAW) and Perdew-Burke-Ernzerhof (PBE) generalized gradient approximation (GGA), respectively.[2,3] The plane wave cutoff energy was set as 450 eV. The convergence tolerance for energy change, max force, and max displacement are 1.0×10^{-5} eV/atom, 0.03 eV/Å, and 0.002 Å, respectively. The first Brillouin zone was sampled with 1×1×1 k-points for both calculations. The van der Waals interactions between COF and organic ligands were considered by Grimme (DFT-D) method[4].

Computational simulation studies of gases adsorption:

Grand Canonical Monte Carlo (GCMC) simulations were performed using the Sorption module of Materials Studio 8.0 package. The Locate and Metropolis methods were employed for predict the possible binding sites of C_2H_2, CO_2 onto the framework. The unit cell framework of COFs was assembled from simulated X-ray diffraction data. In the simulation process, all gas molecules and frameworks are regarded as rigid bodies, and periodic boundary conditins are applied in all three directions. All parameters including the partial charges were assigned by the COMPASS force field embedded in the Sorption module.

Dynamic Breakthrough experiments:

The breakthrough separation experiment was conducted in a home-built breakthrough apparatus under ambient conditions (298 K, 1 bar). In a typical breakthrough experiment, the activated TP-TFPB-COF (0.2 g) and TP-NFPB-COF (about 0.21 g) powders were packed into stainless steel column (Φ 6 × 80 mm) and purged with He flow (20 mL/min) for 4 hours at 298 K for the activation process.

2. Synthesis and characterization

2.1. Synthesis of monomers

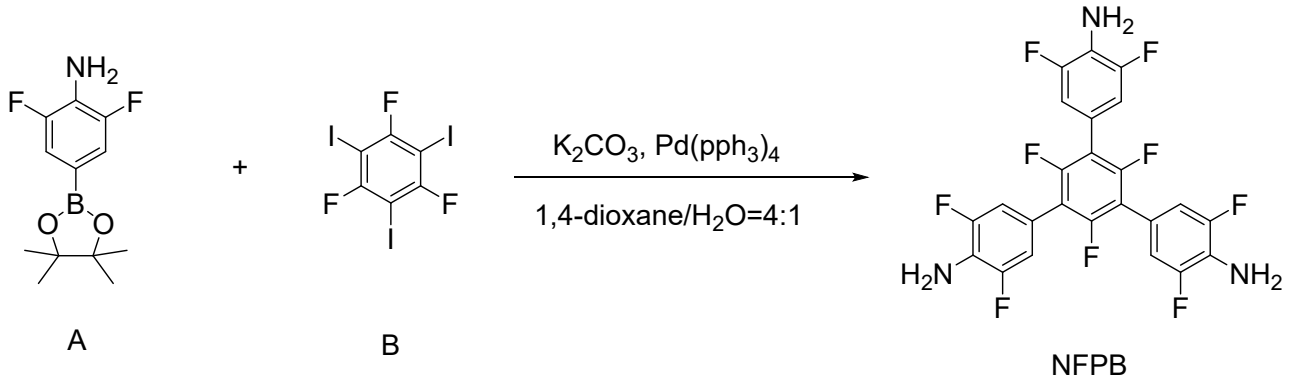

Scheme S1. 5'-(4-amino-3,5-difluorophenyl)-2',3,3'',4',5,5'',6'-heptafluoro-[1,1':3',1''-terphenyl]-4,4''-diamine (**NFPB**). 2,6-difluoro-4-(4,4,5,5-tetramethyl-1,3,2-dioxaborolan-2-yl)aniline (**A**, 3.27 g, 12.8 mmol), 1,3,5-trifluoro-2,4,6-triiodobenzene (**B**, 2.04 g, 4 mmol), K_2CO_3 (2.77 g, 20 mmol), and $Pd(pph_3)_4$ (0.24 g, 0.2 mmol) were mixed in a 250 mL single neck flask, then 1,4-Dioxane (100 mL) and H_2O (25 mL) were added. The mixture was heated at 110 °C for 48 hours under nitrogen atmosphere and then cooled to room temperature, followed by extraction with dichloromethane. After the organic phase was washed with brine and dried over $MgSO_4$, the organic solvent was removed under reduced pressure. NFPB was purified by column chromatography (EA: PE= 1:2) and obtained as a white solid (1.49 g, yield: 73 %). ^{1}H NMR (400 MHz, DMSO-d_6) δ; 7.18 (d, 6 H), 5.55 (m, 6 H).

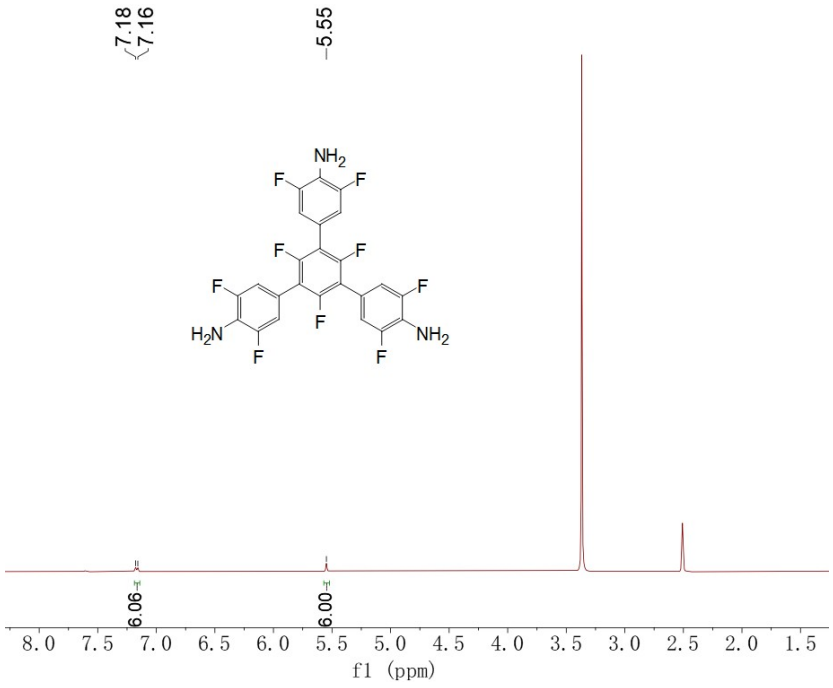

Figure S1. ^{1}H NMR spectrum of NFPB, Solvent peaks of *d*-DMSO (a), H_2O (b).

2.2 Synthesis of TP-TFPB-COF and TP-NFPB-COF

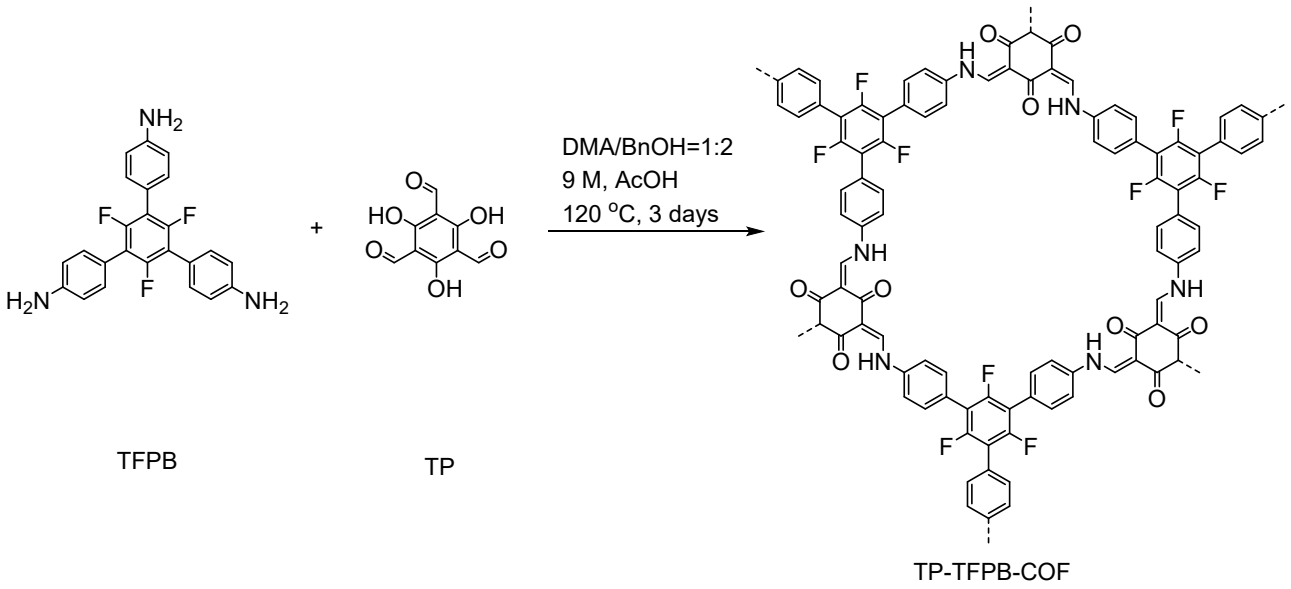

Scheme S2. Synthesis of TP-TFPB-COF: A 10-mL Pyrex tube was charged with TP (12.6 mg, 0.06 mmol), TFPB (24.3 mg, 0.06 mmol) with DMA (0.4 mL) and BnOH (0.8 mL). The mixture was sonicated for 5 minutes to obtain a yellow turbid solution. To this, 9 M acetic acid (0.12 mL) were added as a catalyst. The tube was subsequently cooled to 77 K using a liquid nitrogen bath and subjected to three freeze-pump-thaw cycles for degassing. After sealing under vacuum, the tube was heated at 120 °C for 3 days. Upon cooling to room temperature, a yellow precipitate isolated by centrifugation at 40 *g* (6000 rpm) for 2 minutes, washed with anhydrous acetone, and subjected to solvent exchange with anhydrous tetrahydrofuran three times. The sample was dried under vacuum at 80 °C 12 hours to yield a yellow powder (27.19 mg, 73.71% isolated yield).

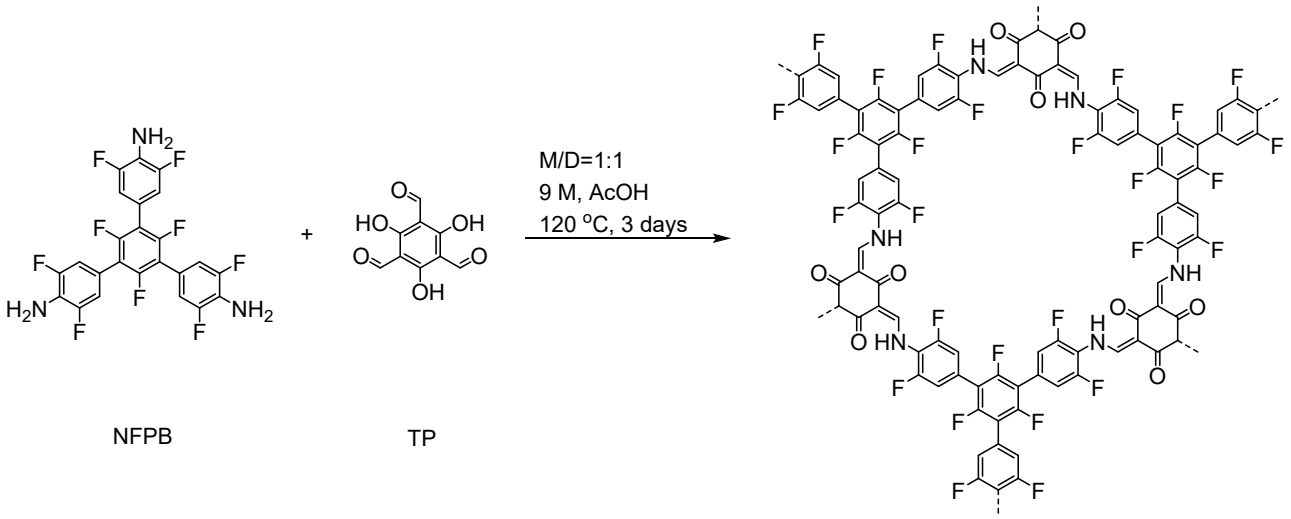

NFPB TP TP-NFPB-COF

Scheme S3. Synthesis of TP-NFPB-COF: A 10-mL Pyrex tube was charged with TP (12.6 mg, 0.06 mmol), NFPB (30.8 mg, 0.06 mmol) with Mesitylene (0.5 mL) and 1,4-Dioxane (0.5 mL). The mixture was sonicated for 5 minutes to obtain a yellow turbid solution. To this, 9 M acetic acid (0.1 mL) were added as a catalyst. The tube was subsequently cooled to 77 K using a liquid nitrogen bath and subjected to three freeze-pump-thaw cycles for degassing. After sealing under vacuum, the tube was heated at 120 °C for 3 days. Upon cooling to room temperature, a yellow precipitate was isolated through centrifugation at 40 *g* (6000 rpm) for 2 minutes, washed with anhydrous acetone, and subjected to solvent exchange with anhydrous tetrahydrofuran three times. The sample was dried under vacuum at 80 °C 12 hours to yield a yellow powder (30.91 mg, 71.24% isolated yield).

2.3. Characterization of TP-TFPB-COF and TP-NFPB-COF

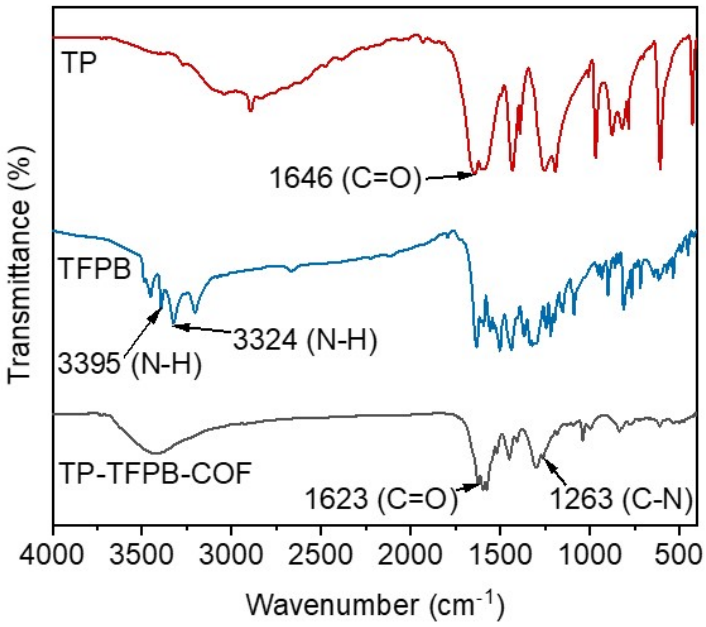

Figure S2. FT-IR spectra of TP, TFPB, and TP-TFPB-COF.

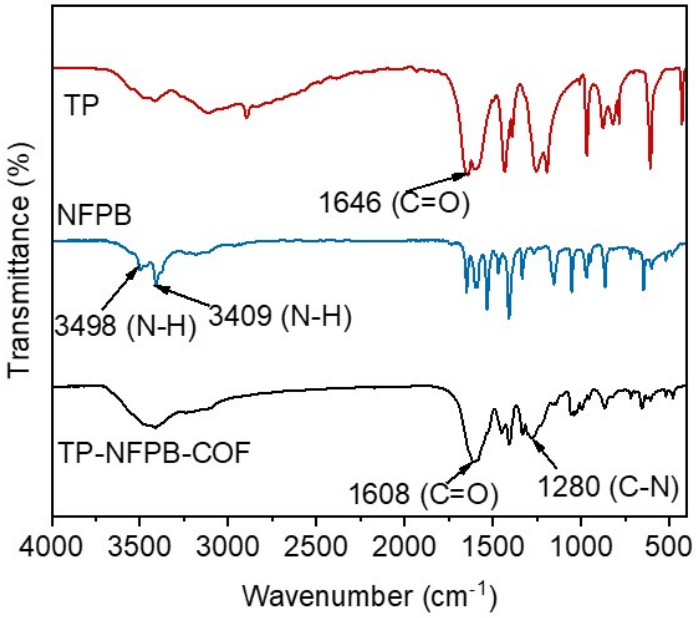

Figure S3. FT-IR spectra of TP, NFPB, and TP-NFPB-COF.

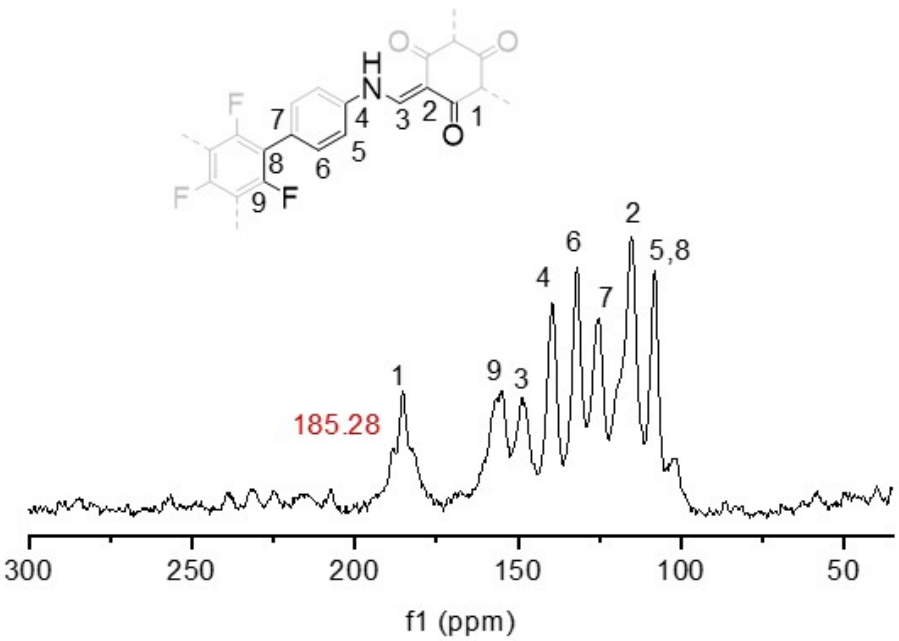

Figure S4. Solid-state ^{13}C CP/MAS NMR spectrum of TP-TFPB-COF.

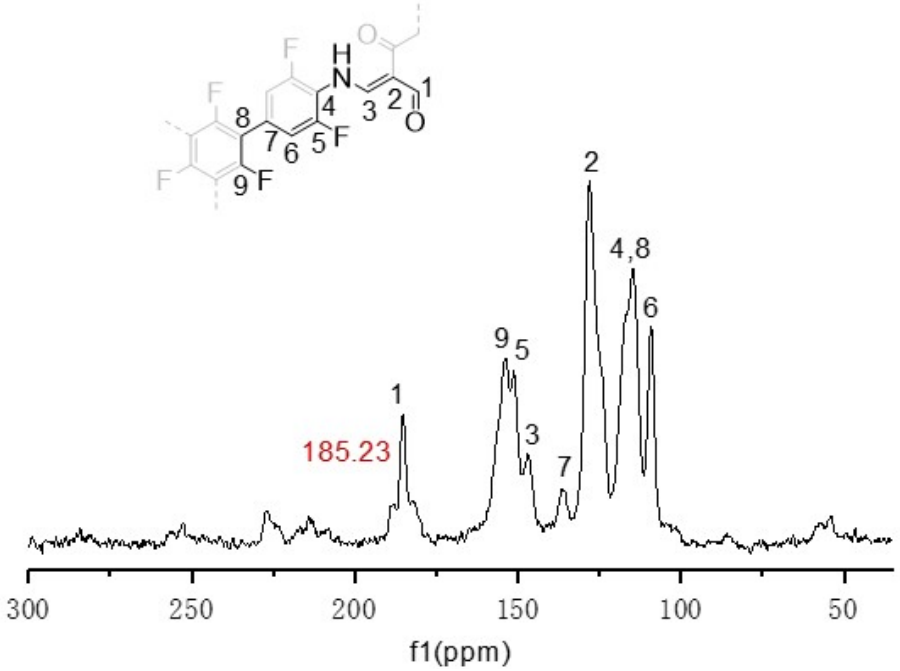

Figure S5. Solid-state ^{13}C CP/MAS NMR spectrum of TP-NFPB-COF.

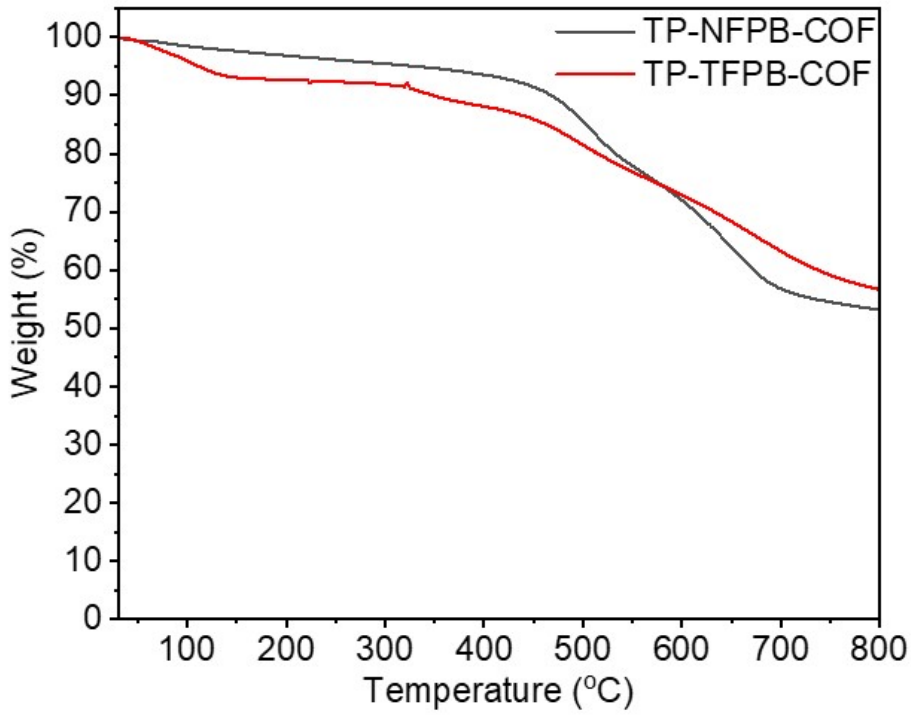

Figure S6. TGA curves of TP-TFPB-COF and TP-NFPB-COF under N_2 atmosphere conditions.

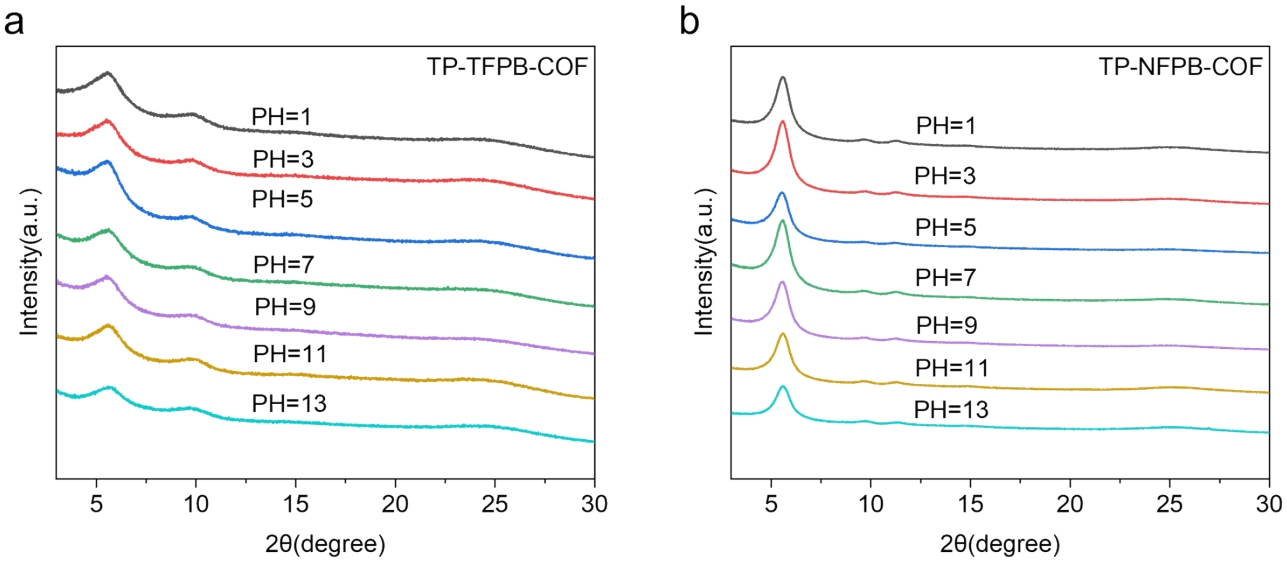

Figure S7. PXRD patterns of (a) TP-TFPB-COF and (b) TP-NFPB-COF after treatment under different pH conditions.

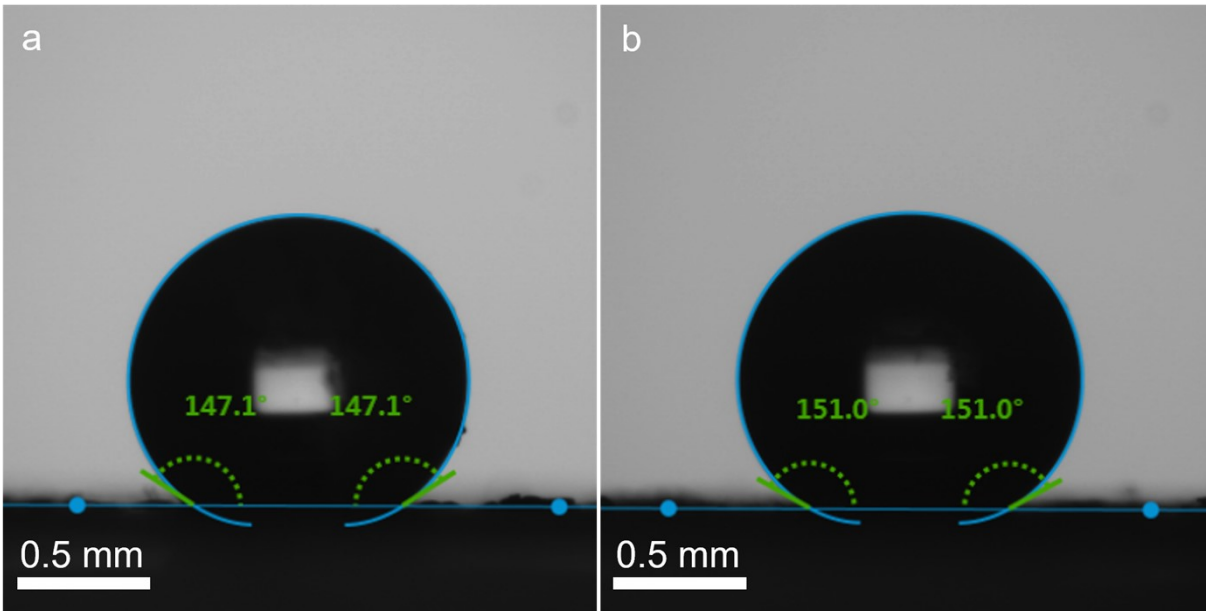

Figure S8. Water contact angle measurements of (a) TP-TFPB-COF and (b) TP-NFPB-COF.

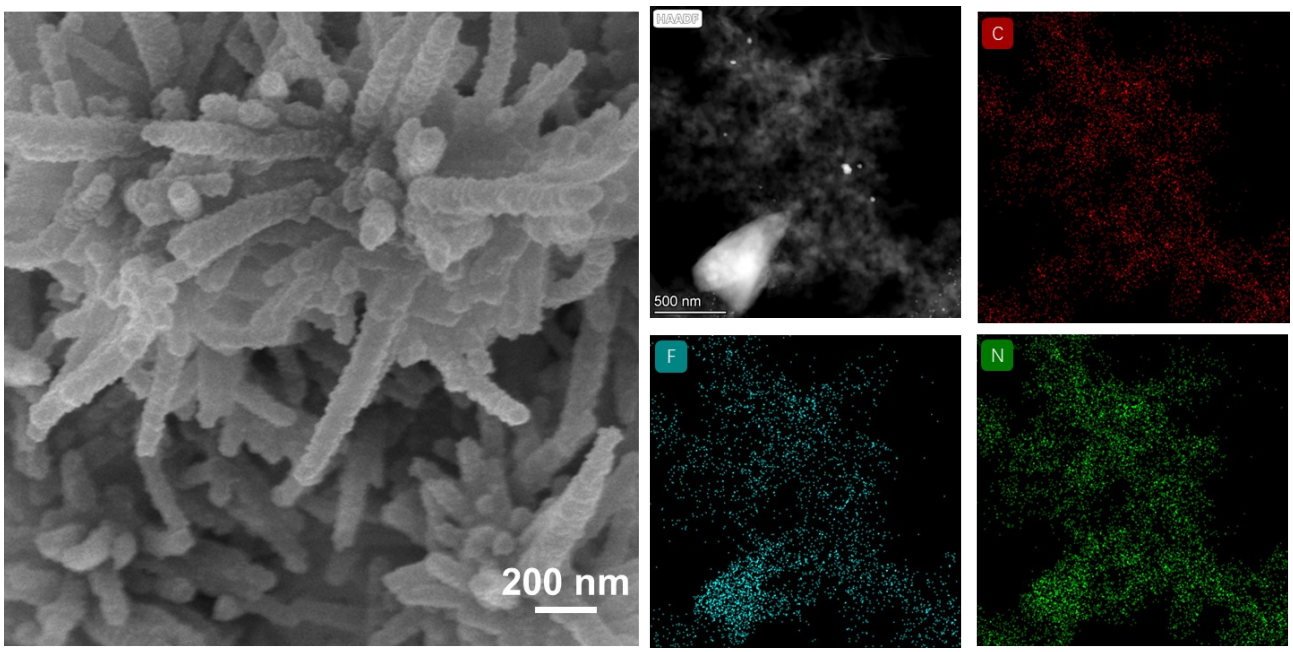

Figure S9. SEM image and elemental mapping of TP-TFPB-COF.

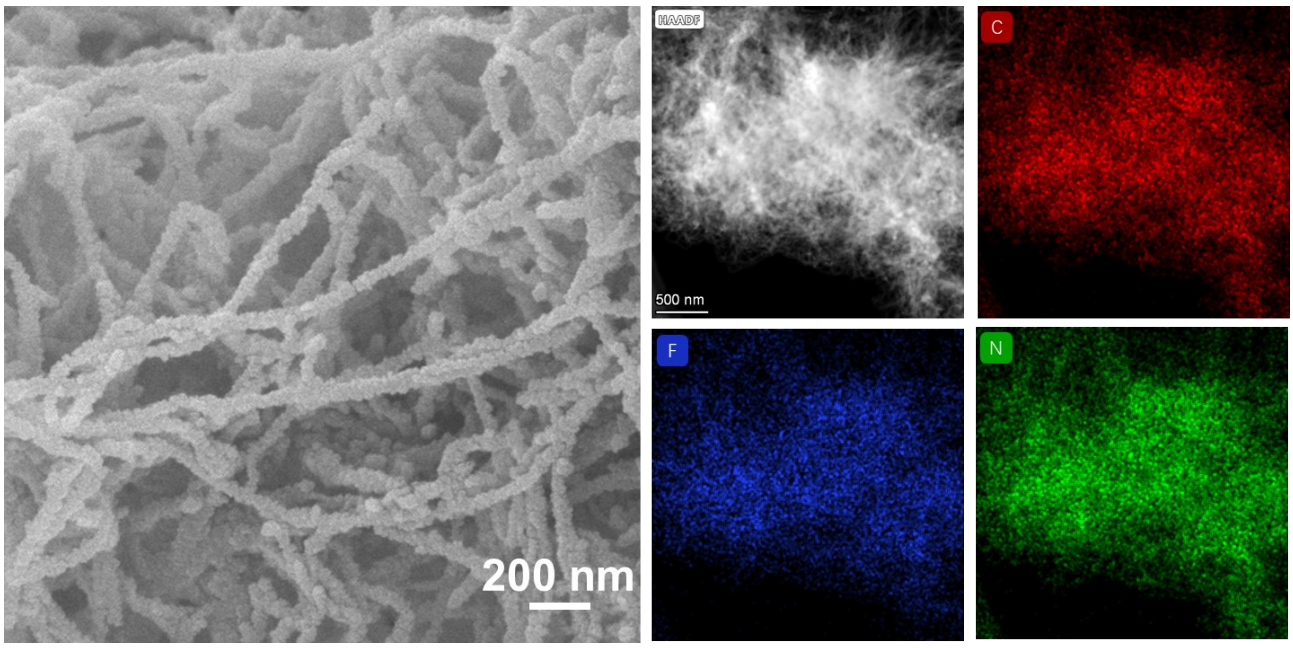

Figure S10. SEM image and elemental mapping of TP-NFPB-COF.

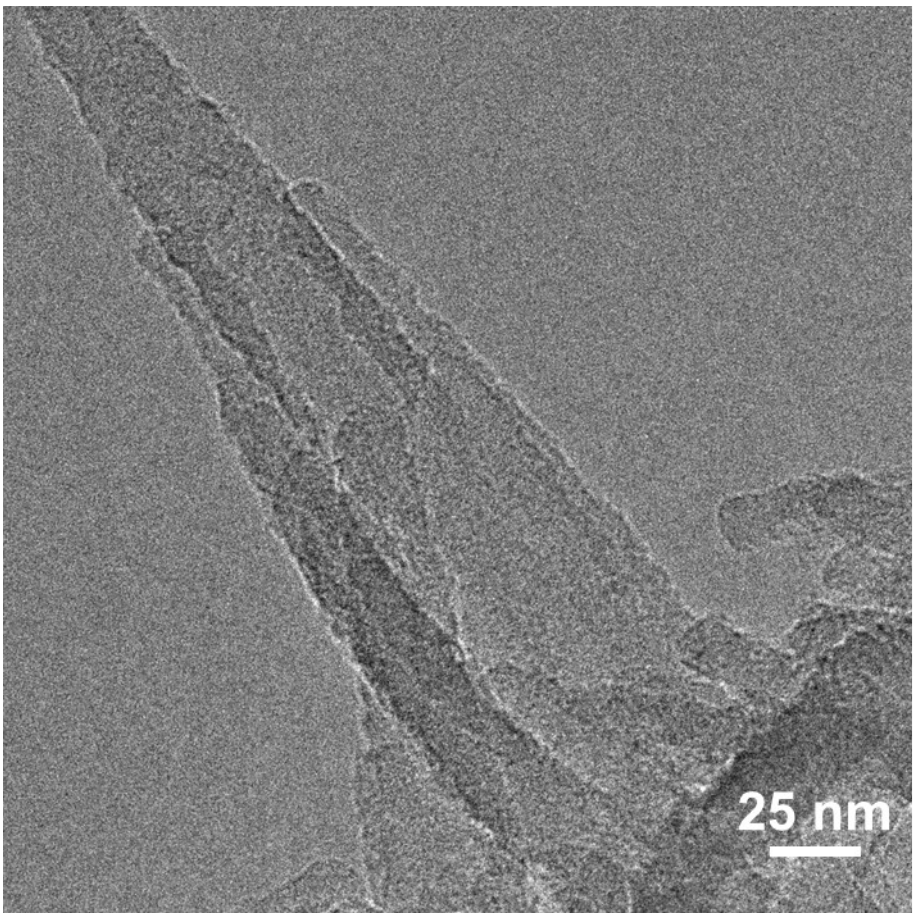

Figure S11. TEM image of TP-TFPB-COF.

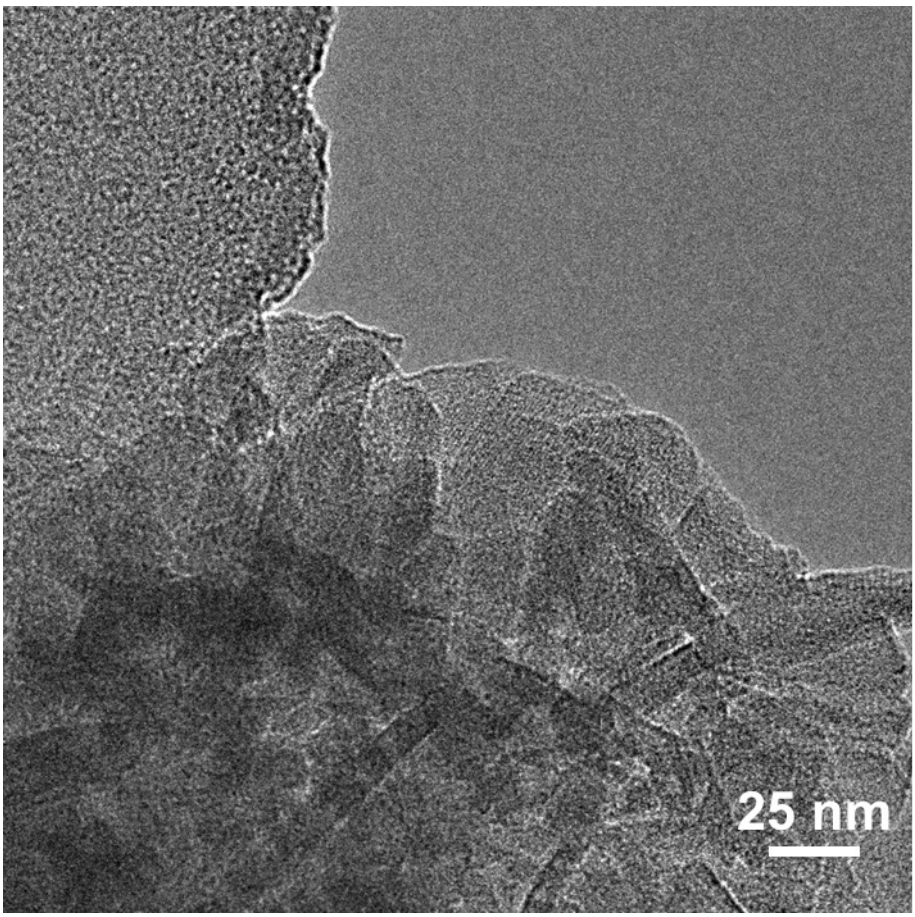

Figure S12. TEM image of TP-NFPB-COF.

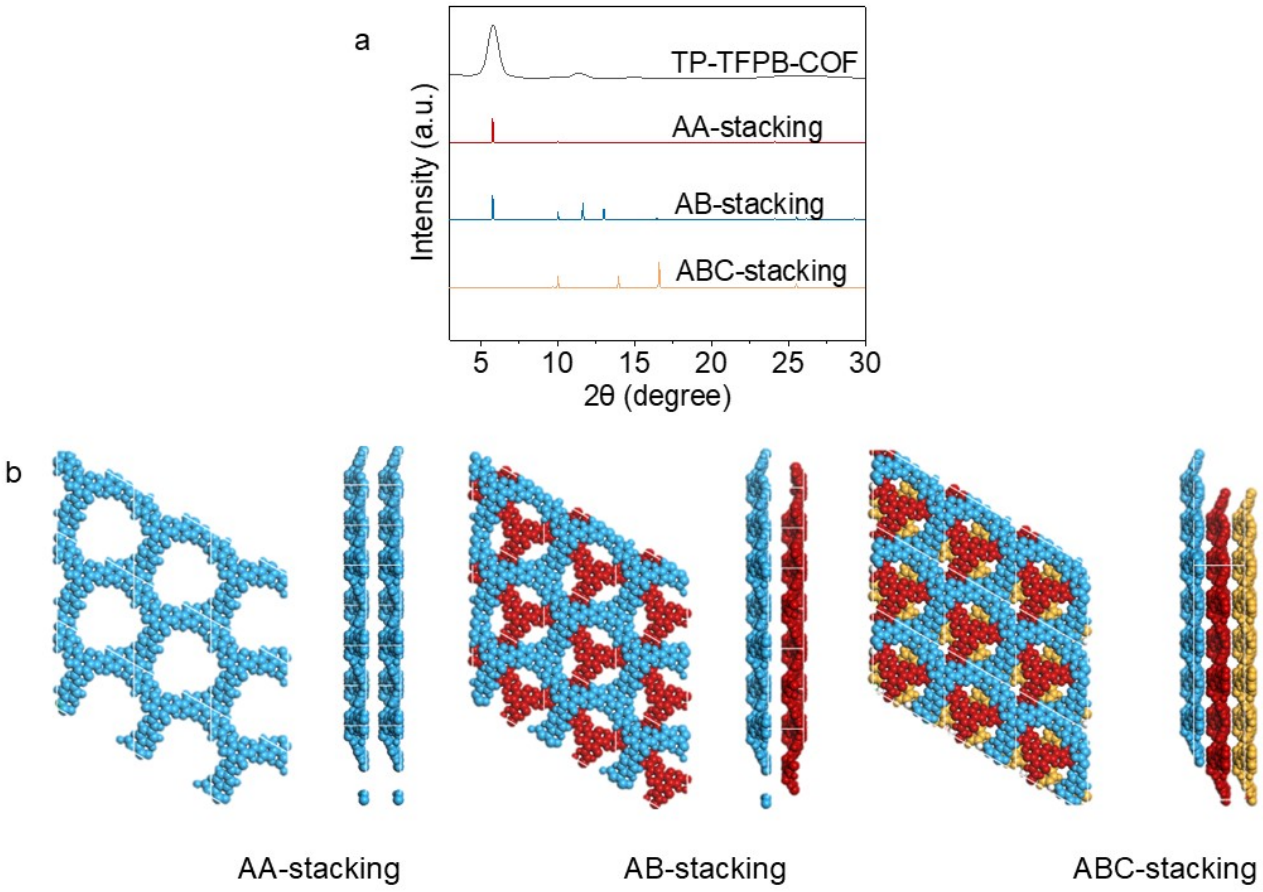

Figure S13. (a) PXRD patterns of TP-TFPB-COF: comparison of the experimental profile with simulated patterns based on AA, AB, and ABC stacking models. (b) Structural models of TP-TFPB-COF illustrating the AA, AB, and ABC stacking arrangements.

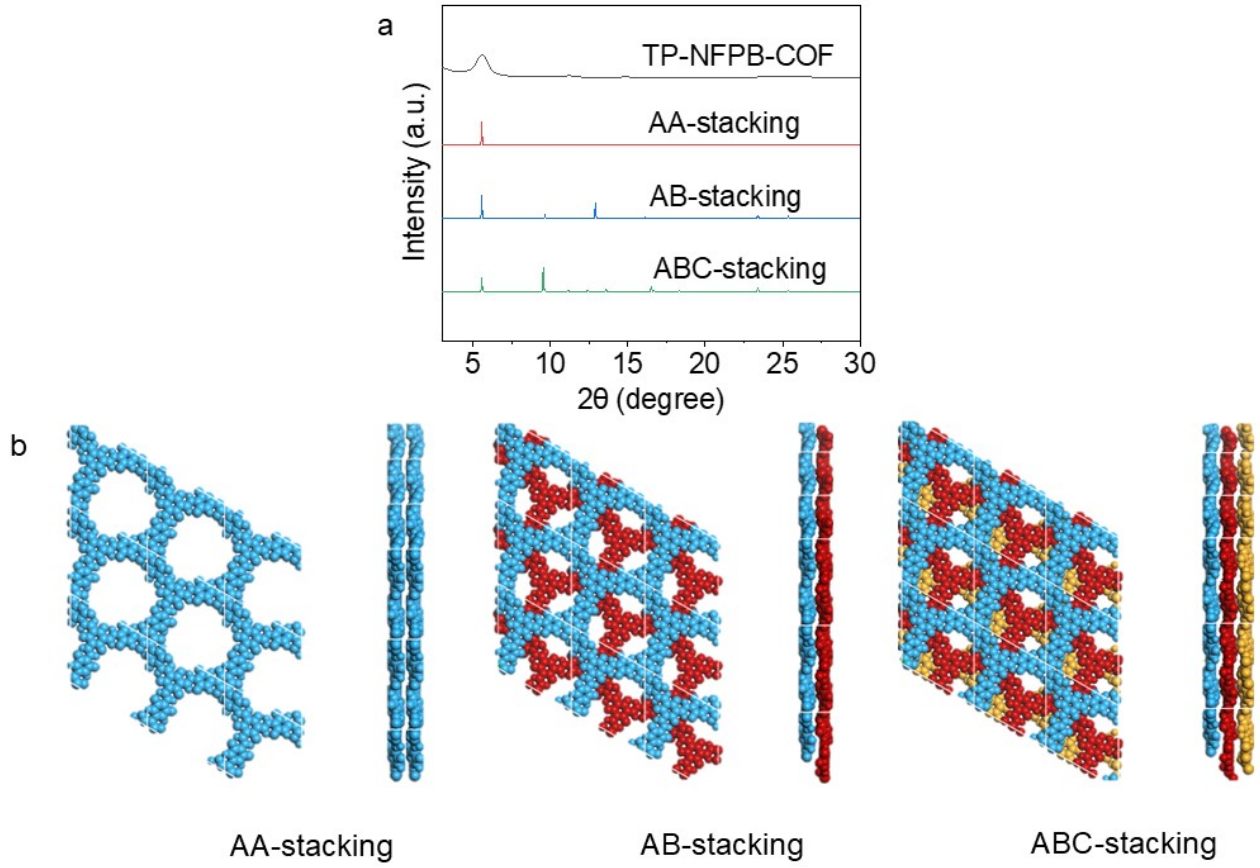

Figure S14. (a) PXRD patterns of TP-NFPB-COF: comparison of the experimental profile with simulated patterns based on AA, AB, and ABC stacking models. (b) Structural models of TP-NFPB-COF illustrating the AA, AB, and ABC stacking arrangements.

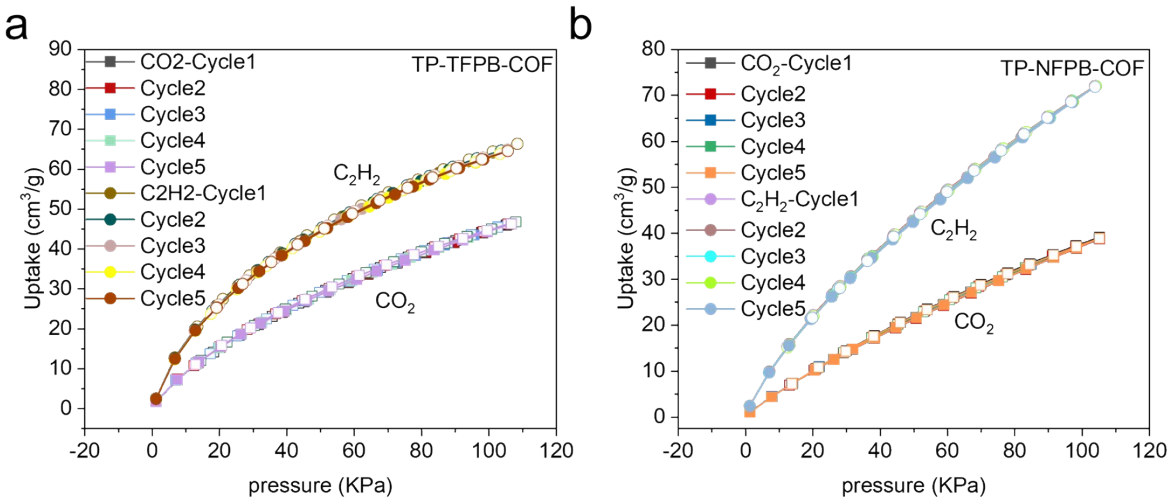

Figure S15. C_2H_2 and CO_2 adsorption isotherms of (a) TP-TFPB-COF and (b) TP-NFPB-COF at 298 K over five adsorption-desorption cycles.

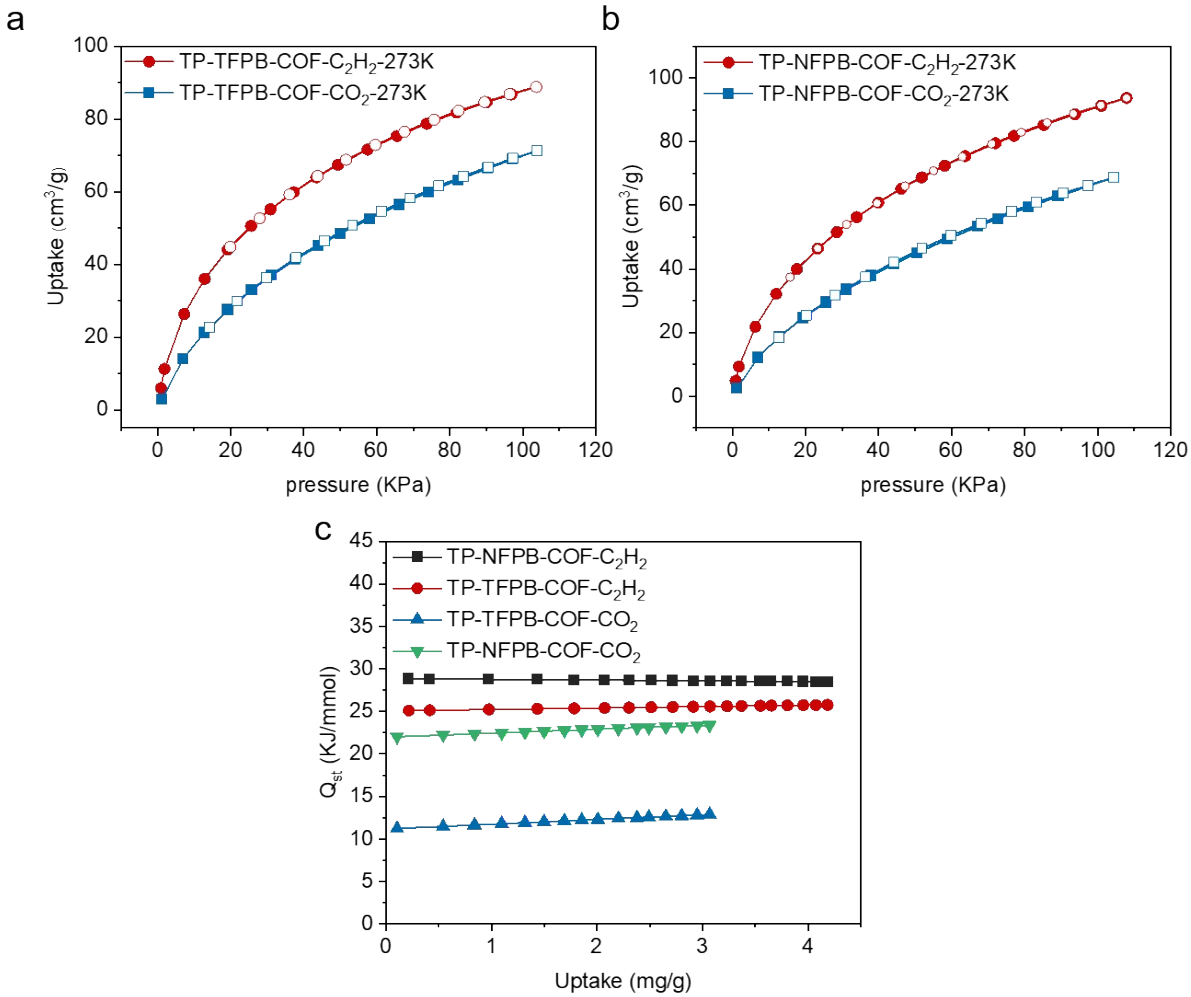

Figure S16. (a,b) C_2H_2 and CO_2 adsorption isotherms for (a)TP-TFPB-COF and (b) TP-NFPB-COF at 273 K. (c) The coverage-dependent adsorption enthalpies (Q_{st}) of C_2H_2 and CO_2 for TP-TFPB-COF and TP-NFPB-COF.

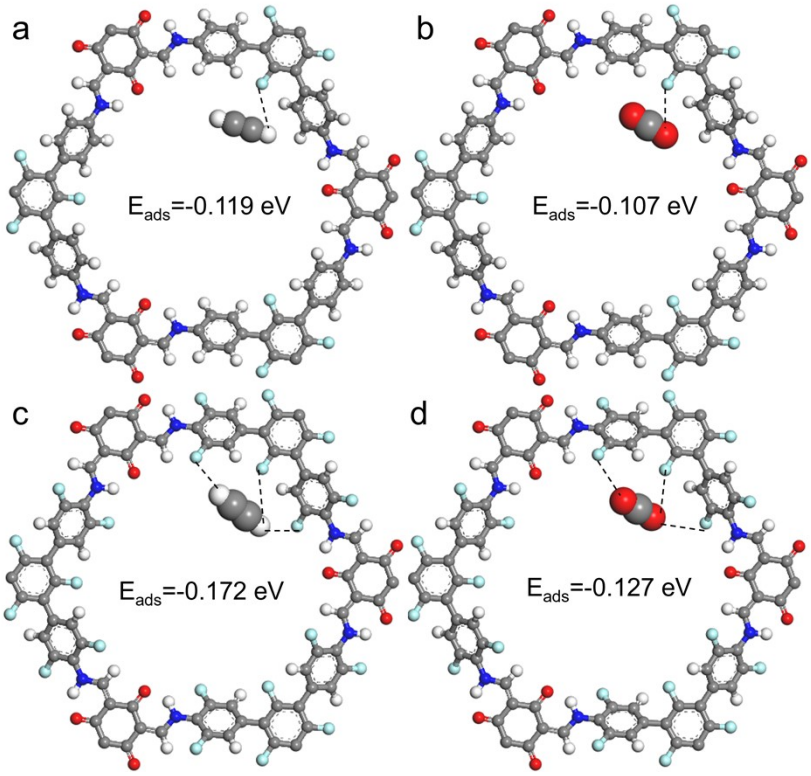

Figure S17. Optimized adsorption configurations and corresponding adsorption energies of C_2H_2 and CO_2 within the nanopores of (a,b) TP-TFPB-COF and (c,d) TP-NFPB-COF, as calculated via density functional theory.

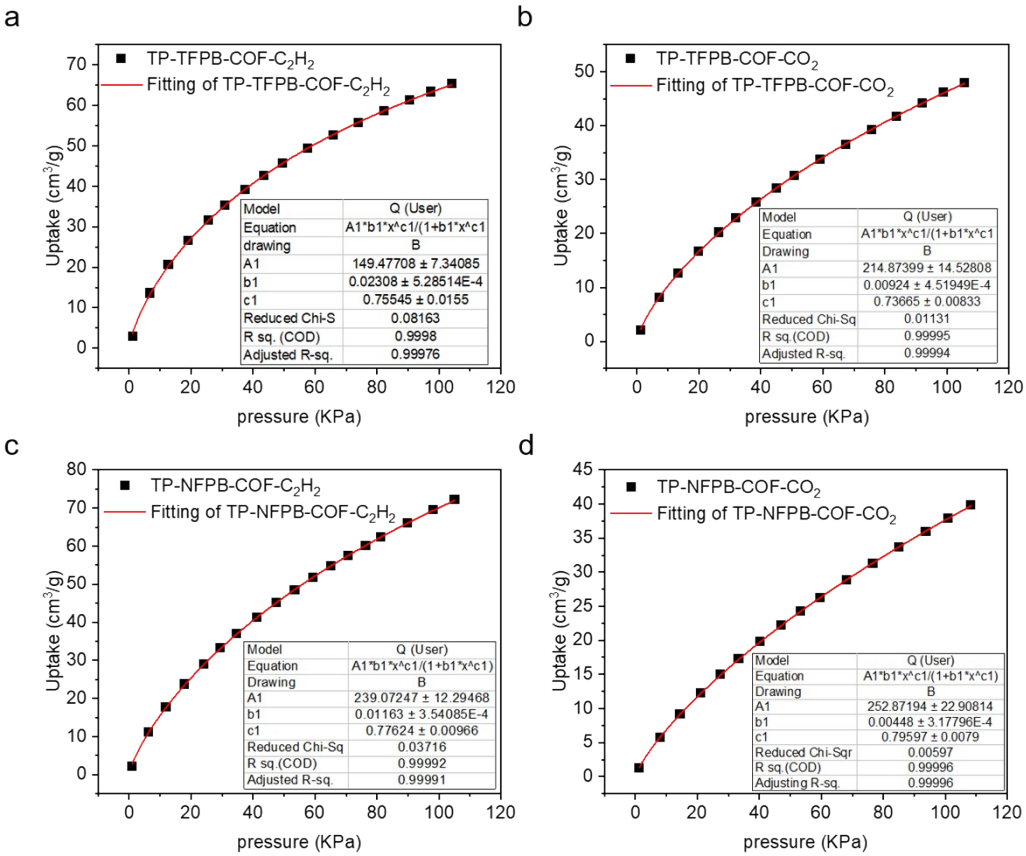

Figure S18. Fitting plots of (a,b) TP-TFPB-COF and (c,d) TP-NFPB-COF for the IAST calculations.

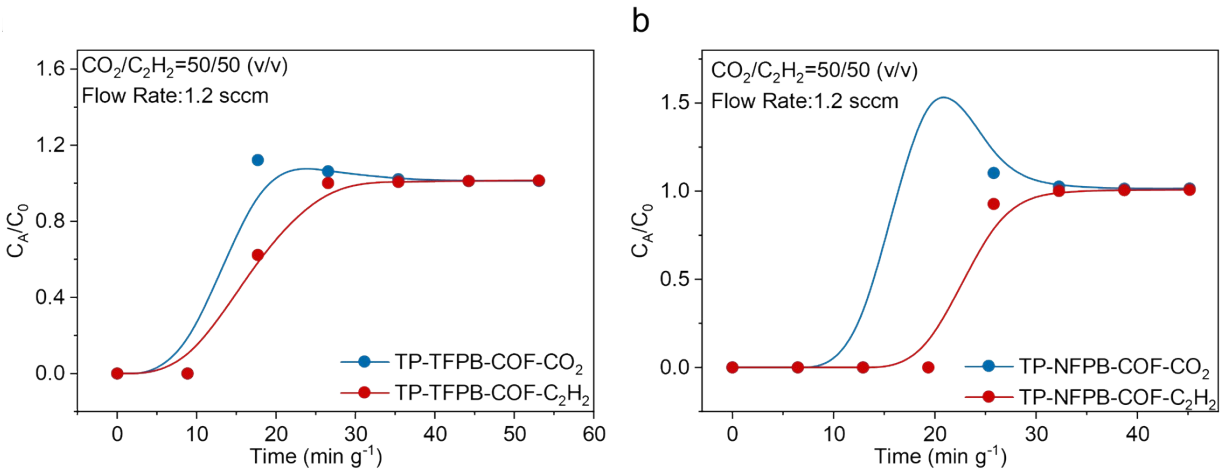

Figure S19. Dynamic breakthrough curves of (a) TP-TFPB-COF and (b) TP-NFPB-COF for an equimolar C_2H_2 and CO_2 mixture at a total flow rate of 1.2 ml min^{-1}.

Table S1. Unit cell parameters and fractional atomic coordinates of TP-TFPB-COF derived from structural optimization based on AA stacking with hcb topology.

Space group		*P3*	
Calculated unit cell		*a* = 17.65 Å, *b* = 17.65 Å, *c* = 3.80 Å *α* = 90.0000°, *β* = 90.0000°, *γ* = 120.0000°	
Atoms	X	Y	Z
C1	0.75221	0.36807	0.55117
C2	0.71786	0.4192	0.55052
O3	0.83585	0.40274	0.55438
C4	0.77424	0.50878	0.55162
N5	0.74914	0.56109	0.51778
C6	0.81516	0.78258	0.4299
C7	0.76725	0.6972	0.43342
C8	0.80167	0.6485	0.5207
C9	0.88568	0.68668	0.61059
C10	0.93386	0.77212	0.61224
C11	0.89964	0.82192	0.52037
C12	0.95124	0.91348	0.51979
F13	0.92141	0.64188	0.70457
F14	0.68641	0.66128	0.34537
C15	0.91534	0.96305	0.51977
H16	0.71789	0.41925	0.22493
H17	0.84449	0.53497	0.58389
H18	0.78499	0.82147	0.35156
H19	1.00304	0.80325	0.68977
H20	0.84429	0.93321	0.51974

Table S2. Unit cell parameters and fractional atomic coordinates of TP-NFPB-COF derived from structural optimization based on AA stacking with hcb topology.

Space group		*P3*	
Calculated unit cell		*a* = 18.8987 Å, *b* = 18.8987 Å, *c* = 3.4925 Å *α* = 90.0000°, *β* = 90.0000°, *γ* = 120.0000°	
Atoms	X	Y	Z
C1	0.72035	0.42371	0.50583
C2	0.62996	0.38651	0.50761
O3	0.59911	0.42993	0.51081
C4	0.7714	0.50481	0.50207
C5	0.0355	0.9512	0.50549
C6	0.95012	0.91383	0.50554
C7	0.89733	0.82263	0.50467
C8	0.81288	0.78475	0.41977
C9	0.76395	0.69971	0.42066
C10	0.79739	0.65004	0.49921
C11	0.88112	0.68656	0.58428
C12	0.93037	0.77163	0.58896
N13	0.74441	0.56314	0.49156
F14	0.91559	0.64053	0.67158
F15	0.68323	0.66516	0.33743
F16	0.77693	0.82923	0.32803
F17	0.01019	0.80333	0.68464
H18	0.84028	0.53036	0.50736
H19	0.05336	0.92665	0.76378
H20	0.04821	0.92453	0.23893
H21	0.95007	0.91374	0.83195
H22	0.67813	0.54214	0.47634

Table S3. Summary of C_2H_2 and CO_2 adsorption capacities and C_2H_2/CO_2 (50/50, v/v) IAST selectivities for various porous materials at 298 K and 100 kPa.

Porous materials	q, C_2H_2 ($mmol \cdot g^{-1}$)	q, CO_2 ($mmol \cdot g^{-1}$)	C_2H_2/CO_2 selectivity	Refs.
TP-TFPB-COF	2.66	1.95	2.04	This work
TP-NFPB-COF	2.94	1.62	2.86	This work
ZJUT-3	1.41	0.65	3.2	5
BNOF-1	4.62	3.06	3.1	6
TFT COF	1.61	1.27	4.18	7
TTA-HFB-COF	2.09	1.60	1.82	8
TpPa-F	4.78	2.52	3.3	9
FJU-36a	2.13	1.44	2.8	10
NKCOF-12	3.5	2.5	2.3	11
USTB-25-3D	2.57	1.28	2.4	12

References

1. Materials Studio; Accelrys: San Diego.
2. M. Torrenta, N. A. W. Holzwarthb, F. Jolleta, D. Harrisb, N. Lepleyb, X. Xub, Comput. Phys. Commun., 2010, **181**, 1862–1867.
3. J. P. Perdew, K. Burke, M. Ernzerhof, Phys. Rev. Lett., 1996, **77**, 3865.
4. S. Grimme, S. Ehrlich, L. Goerigk, J. Comput. Chem., **32**, 1456-1465.
5. C. Gong, H. Wang, G. Sheng, X. Wang, X. Xu, J. Wang, X. Miao, Y. Liu, Y. Zhang, F. Dai, L. Chen, N. Li, G. Xu, J. Jia, Y. Zhu and Y. Peng, *Angew. Chem. Int. Ed.*, 2022, **61**, e202204899.
6. W. Wang, L. Wang, F. Du, G. D. Wang, L. Hou, Z. Zhu, B. Liu and Y. Y. Wang, *Chem. Sci.*, 2023, **14**, 533-539.
7. J. Chen, C. Jiang, Z. Xing, J. Li, F. Dai and Y. Peng, *New J. Chem.*, 2023, **47**, 6759-6764.
8. Y. Lu, B. Zhang, Y. Fu, H. Dong, H. Liao, Q. Qi, M. Zhang, X. Hu, X. Zhao, S. Chen and L. Wang, *J. Mater. Chem. A*, 2025, **13**, 22445-22452.
9. S. Liu, C. Hao, C. Meng, S. Liu, W. Zhai, Q. Zhu, W. Li, S. Wei, Z. Wang and X. Lu, *ACS Appl. Nano Mater.*, 2023, **6**, 12124-12131.
10. L. Liu, Z. Yao, Y. Ye, L. Chen, Q. Lin, Y. Yang, Z. Zhang and S. Xiang, *Inorg. Chem.*, 2018, **57**, 12961-12968.
11. P. Zhang, Z. Wang, Y. Yang, S. Wang, T. Wang, J. Liu, P. Cheng, Y. Chen and Z. Zhang, *Sci. China Chem.*, 2022, **65**, 1173-1184.
12. B. Yu, S. Geng, X. Ding, X. Zhou, Y. Jin, H. Wang, X. Wang, T. Zheng, Z. Zhang and J. Jiang, *Chem.*, 2024, **10**, 2170-2179.